Observation of the correlated O $^3P_{j1}$, $^3P_{j2}$ state distribution from the predissociation of O_2 B $^3\Sigma_u^-$

David J. Leahy, Douglas R. Cyr [1], David L. Osborn [2] and Daniel M. Neumark [3]
Chemistry Department, University of California, Berkeley, CA 94720, USA
and Chemical Sciences Division, Lawrence Berkeley Laboratory, Berkeley, CA 94720, USA

Received 27 September 1993; in final form 21 October 1993

A fast beam photofragment translational spectroscopy study of the predissociation of the O_2 B $^3\Sigma_u^-$ state is presented. A 5 keV beam of vibrationally excited O_2 X $^3\Sigma_g^-$ is prepared via photodetachment of O_2^-. The B $^3\Sigma_u^-$ ($v'=7$)←X $^3\Sigma_g^-$ ($v''=4$) transition of the Schumann–Runge band is then excited, resulting in predissociation to two O ^3P_j atoms. We determine the photofragment kinetic energy angular distribution using a time- and position-sensitive detector. Our energy resolution (10 meV) is sufficient to resolve the energy splittings of the O atom spin–orbit levels, enabling us to determine the correlated (j_1, j_2) fine structure distribution for the photofragments. These results do not appear to be consistent with predictions based on a recent model of O_2 B $^3\Sigma_u^-$ state predissociation.

1. Introduction

The Schumann–Runge B $^3\Sigma_u^-$ ← X $^3\Sigma_g^-$ system of molecular oxygen, the first far ultraviolet molecular spectrum to be observed [1], plays a central role in the photochemistry of the Earth's upper atmosphere. Predissociation from the O_2 B $^3\Sigma_u^-$ state is one of the main sources of O ^3P_j atoms in the atmosphere above 60 km. Perhaps more importantly, the B $^3\Sigma_u^-$ (v')← X $^3\Sigma_g^-$ ($v''=0$) vibronic bands are primarily responsible for the absorption of solar radiation in the wavelength range from 175 to 205 nm. Knowledge of the strength of this absorption over this wide range is crucial for the modeling of the penetration of far ultraviolet light into the atmosphere. In addition to the oscillator strengths of the specific transitions, the natural linewidths of rovibrational levels of the predissociative B $^3\Sigma_u^-$ state are required for successful modeling of the penetration depth of this photochemically important radiation [2]. For this reason, the need for a quantitative description of B $^3\Sigma_u^-$ state predissociation dynamics remains an important problem. Although the long vibrational progressions of the Schumann–Runge band have been carefully mapped out [3–5], it has been more difficult to elucidate the detailed B $^3\Sigma_u^-$ state predissociation dynamics. In this Letter, we report a high-resolution photofragment translation spectroscopy study of the O_2 B $^3\Sigma_u^-$ ($v'=7$) state that yields considerable insight into the predissociation mechanism.

The complexity of the B $^3\Sigma_u^-$ state predissociation mechanism arises from coupling to at least four repulsive states: namely, the $^3\Pi_u$, $^1\Pi_u$, $^5\Pi_u$, and 2 $^3\Sigma_u^+$ states [6,7]. These four curves all have comparable coupling strengths to the B $^3\Sigma_u^-$ state, primarily through spin–orbit interactions. The majority of the effort to disentangle these interactions has been via spectroscopic investigation of the line positions and line widths of the Schumann–Runge bands. Lewis et al. [4] and Parkinson and co-workers [8,9] have modeled the strong rovibrational state dependence of the dissociation dynamics by fitting the coupling strengths and potential curves of the $^3\Pi_u$, $^1\Pi_u$, $^5\Pi_u$, and 2 $^3\Sigma_u^+$ states to their large body of measurements of line positions and widths [3–5]. Wodtke and co-workers have analyzed the spin–ro-

[1] NSERC (Canada) 1967 Predoctoral Fellow.
[2] NDSEG Predoctoral Fellow.
[3] NSF Presidential Young Investigator and Camille and Henry Dreyfus Teacher-Scholar.

SSDI 00009-2614(93)E1297-T

tation state-resolved laser-induced fluorescence from some high vibrational levels of the $B\,^3\Sigma_u^-$ state [10,11]. Their results provided some new insight into the dissociation mechanism, particularly with regard to the importance of the orbit–rotation interaction between the $B\,^3\Sigma_u^-$ and the $^3\Pi_u$ states. Wodtke's work and the recent results of Cosby et al. [12] suggest that some uncertainty remains regarding both the strength of the coupling between the $B\,^3\Sigma_u^-$ state with the repulsive curves and the location of the curve crossings.

The $B\,^3\Sigma_u^-$ state dissociation mechanism can also be probed by characterizing the fine structure distribution of the O atom fragments. For example, Huang and Gordon [13] used 157 nm light to excite O_2 to the Schumann–Runge $B\,^3\Sigma_u^-$ continuum above the ^1D, $^3P_2$ dissociation limit, and measured the spin–orbit state distribution of the O^3P_j atoms. They found the $j=2$ level to be the dominant product by far (93%), and from this concluded that they were observing primarily direct dissociation on the $B\,^3\Sigma_u^-$ state surface to $O\,^1D + O\,^3P_2$ products. In a study more closely related to the work presented here, Kawasaki and co-workers used resonance-enhanced multiphoton ionization to measure the (uncorrelated) spin–orbit distribution of the two $O\,^3P_j$ atoms resulting from predissociation of the $v'=4$ level of the $B\,^3\Sigma_u^-$ state [14]. Kawasaki has also reported results following direct dissociation in the Herzberg $A\,^3\Sigma_u^+$ continuum [15].

One can learn considerably more about the $B\,^3\Sigma_u^-$ state predissociation dynamics by measuring the *correlated* (j_1, j_2) distribution for the two $O\,^3P_j$ atoms, and these are reported for the first time in this Letter. The value of such a measurement derives from the correlations between each potential energy curve involved in the dissociation process and the asymptotic (j_1, j_2) states of the recoiling O atoms [16]. Thus, a measurement of the correlated fine structure distribution should aid in identifying the participating states, at least in the adiabatic limit. Because the Schumann–Runge bands are vibrationally and (partially) rotationally resolved, one can, in principle, observe how the fine structure distribution varies with vibrational and rotational quantum number, and thus map out the contributions of the various repulsive states.

An additional feature of these measurements is that they are sensitive to long-range exit channel interactions that occur en route to dissociation. One can adiabatically correlate the molecular states to the asymptotic $O\,^3P_{j_1} + O\,^3P_{j_2}$ levels, but at long range (internuclear coordinate R much larger than R_e), the energy gaps between the (non-degenerate) limits are only a few hundred wavenumbers, i.e. some two orders of magnitude smaller than the kinetic energy of the recoiling atoms. (The excited $^3P_1$ and $^3P_0$ states lie 158 and 226 cm^{-1} above the $^3P_2$ ground state, respectively.) We therefore expect some nonadiabatic curve crossings to occur among the repulsive surfaces, particularly in the "recoupling region", the range of internuclear distances where neither Hund's case (c) nor Hund's case (a) is appropriate for describing the coupling of the various angular momenta [16,17]. Evidence for such effects has already been observed in the previous measurements of the $O\,^3P_j$ spin–orbit state distributions following O_2 dissociation [13–15], but again, the correlated measurements presented here provide a more direct probe of these exit-channel interactions.

In our work, we prepared vibrationally excited O_2 by photodetachment of O_2^-, excite the $B\,^3\Sigma_u^-$ $(v'=7) \leftarrow X\,^3\Sigma_g^-$ $(v''=4)$ transition, and then determine the correlated fine structure distribution and product angular distribution via a high-resolution photofragment translational spectroscopy technique. Fig. 1 shows the potential energy curves of the electronic states of O_2^- and O_2 that are involved in our excitation scheme. Also shown in fig. 1 are the four repulsive curves that couple to the $B\,^3\Sigma_u^-$ state, causing predissociation to the $^3P_{j_1}$, $^3P_{j_2}$ limit. We find that the dominant (j_1, j_2) product state, representing 55% of the total signal, is the (2, 1) limit, which is correlated which is correlated adiabatically to the $^3\Pi_u$ and $^1\Pi_u$ surfaces [13]. An additional 7% of the events belonged to the (2, 2) limit, which is not correlated adiabatically to any surface that intersects the $B\,^3\Sigma_u^-$ state. We briefly discuss the implication of these results in terms of simple models of diatomic photodissociation.

2. Experiment

A description of our application of fast beam photofragment translational spectroscopy to the study of

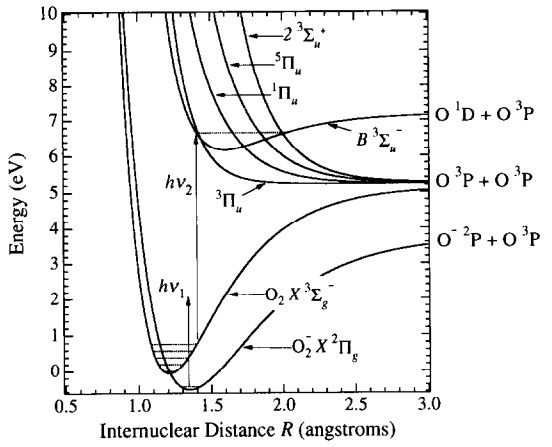

Fig. 1. Schematic of selected potential energy surfaces of O_2^- and O_2. The vertical arrows depict the two photoabsorption processes involved in this experiment: $h\nu_1$ affects the photodetachment step, and $h\nu_2$ excites the $O_2\,B\,^3\Sigma_u^-$ $(v'=7) \leftarrow X\,^3\Sigma_g^-$ $(v''=4)$ transition. Also shown are the four repulsive curves responsible for the predissociation of the $B\,^3\Sigma_u^-$ state.

free radical photodissociation has been published recently [18]. Briefly, we prepare a fast beam (5 keV) of mass-selected, rotationally cold neutral O_2 molecules via photodetachment of the negative ion precursor O_2^-. The resulting neutrals are electronically excited to the $B\,^3\Sigma_u^-$ state. The $B\,^3\Sigma_u^-$ state proceeds to predissociate within a few picoseconds. We observe the arrival of pairs of O atoms *in coincidence* with our recently developed time- and position-sensitive detector [18].

The negative ion source is similar in design to that developed by Lineberger and co-workers [19]. We expand neat O_2 with a stagnation pressure of 20 psig. The expansion crosses a beam of 1 keV electrons, creating a plasma. Negative ions are formed in the continuum flow region and are cooled in the supersonic expansion. The negative ions are accelerated to a laboratory energy of 5 keV and mass selected by the Bakker time-of-flight method [20]. The resulting negative ion packets are photodetached with the output of an excimer-pumped tunable dye laser. By operating the dye laser at 480 nm (2.58 eV), we photodetach the molecules well above the detachment threshold of 0.45 eV [21,22]. This results in the formation of vibrationally excited $O_2\,X\,^3\Sigma_g^-$ levels as well as some $O_2\,a\,^1\Delta_g$. The vibrational state distributions are governed by the Franck–Condon factors between the $O_2^-\,X\,^2\Pi_g$ anion and neutral O_2. Normally, we avoid vibrational excitation of the neutral species by detaching at or near threshold [23,24]. However, for the study of the Schumann–Runge $B\,^3\Sigma_u^- \leftarrow X\,^3\Sigma_g^-$ band, the vibrational excitation is an important advantage because it permits excitation to the lower vibrational levels of the $O_2\,B\,^3\Sigma_u^-$ state with relatively favorable Franck–Condon factors.

After the residual ions are removed from the beam by a 1 kV/cm deflection field, the O_2 neutral beam is intercepted by a second tunable dye laser pulse. We have selected the overlapped R(3) and P(1) transitions of the $v'=7 \leftarrow v''=4$ band, at 210.23 nm. The vast majority of the neutral beam is not dissociated and continues down the 1.00 m flight region into a 8 mm wide beam block. The photofragments recoil out of the beam, striking the active area of a 46 mm diameter microchannel plate (MCP) detector. For each photodissociation event, we measure the two photofragment positions at the detector and time interval between their arrivals. This information directly yields the magnitude and direction of the center-of-mass recoil velocity vector in three dimensions. This type of coincidence detection scheme was first developed by de Bruijn and Los [25]; our detector is similar in concept, although the position-sensing method is quite different (see ref. [18]).

3. Results

The coincidence events are binned into the signal array $\mathscr{S}(E_T, \theta)$, where E_T is the center-of-mass frame translational energy of the fragments, and θ is the angle between the fragment recoil vector and the electric vector of the linearly polarized dissociation light beam. The raw data are directly related to the true two-dimensional probability distribution $\mathscr{P}(E_T, \theta)$ by

$$\mathscr{P}(E_T, \theta) = \mathscr{S}(E_T, \theta) / \mathscr{D}(E_T, \theta) , \quad (1)$$

where $\mathscr{D}(E_T, \theta)$ is a numerically derived detector acceptance function [18]. This $\mathscr{P}(E_T, \theta)$ distribution can be broken down into separable energy and angle distributions,

$$\mathscr{P}(E_T, \theta) = P(E_T)[1 + \beta(E_T) P_2(\cos\theta)] , \quad (2)$$

where $P(E_T)$ represents the angle-integrated energy

distribution, and $\beta(E_T)$ is the energy dependent anisotropy parameter [26]. We then obtain $\beta(E_T)$ and $P(E_T)$ from a least-squares fit to the differential distribution $\mathscr{P}(E_T, \theta)$.

The circles in fig. 2 represent the resulting $P(E_T)$ distribution. The distribution consists of a central peak, which is about 10 meV wide (fwhm), and smaller, partially resolved peaks to either side. This structure represents the different (j_1, j_2) asymptotic channels for the two O ^{3}P atoms; the energies of these channels are given in table 1. The relative energy resolution in our kinetic energy release spectra is thus $\Delta E_T/E_T = 0.7\%$. However, the absolute energy calibration of the apparatus is only accurate to about 2%, so the absolute energy calibration is not quite sufficient to assign the spin–orbit limits in fig. 2 directly. However, the peaks were assigned unambiguously by a fitting the data to a set of Gaussian peak shapes, separated by the well-known O ^3P_j splittings [27]. The absolute energy scale and the full width at half maximum (fwhm) were adjusted to find the best overall least-squares fit to the observed $P(E_T)$. The best fit was obtained with all of the spin–orbit limit Gaussian peak shapes having a common fwhm of 10.1 meV. The least-squares fit to the observed $P(E_T)$ is shown as the solid line in fig. 2, and the resulting intensities are listed in the third column of table 1. The excellent agreement between the $P(E_T)$ and the fit implies that the assumption of Gaussian peak shapes was valid.

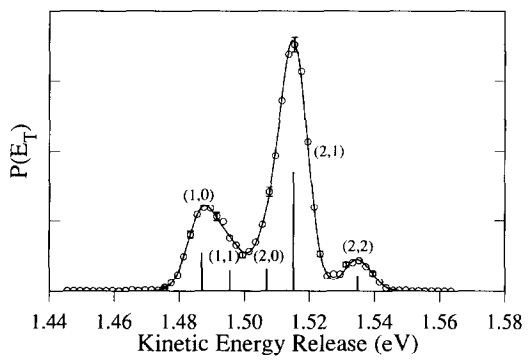

Fig. 2. The translational energy release distribution $P(E_T)$ resulting from the predissociation of O_2 B $^3\Sigma_u^-$ ($v'=7$). (O) Experimental data; (——) results of a fit to these data (see text). Every fourth data point has an error bar, representing the 1σ uncertainty. The sticks denote the positions and intensities of the individual (j_1, j_2) limits as deduced from the fit.

We find that the intense peak in the $P(E_T)$ distribution, contributing over half of the signal, clearly belongs to the (2, 1) channel. The majority of the remaining products are assigned to more energetic limits, especially the (1, 0) channel. A small fraction (7%) of the signal is assigned unambiguously to the lowest energy (2, 2) channel. We observed virtually no intensity in the (0, 0) channel. This result is consistent with the rigorous g/u inversion symmetry conservation; the singly degenerate (0, 0) atomic limit correlates to a gerade molecular state (adiabatically, to the $2\,^5\Sigma_g^+$ state) and is therefore expected to be absent in the predissociation of the B $^3\Sigma_u^-$ state.

Analysis of the angular distributions of recoils in our data for the anisotropy parameter $\beta(E_T)$ gives a

Table 1
The correlated spin–orbit state distribution following the predissociation of O_2 B $^3\Sigma_u^-$ ($v'=7$). The third column contains the relative populations, as determined by the least-squares fit described in the text. The given errors represent 1σ uncertainties. The fourth column contains the expected distribution if the dissociation followed the adiabatic Hund's case (c) curves with the predissociation rates published by Cheung et al. [9]. The fifth column contains the distribution of final states predicted in the statistical limit, while conserving the g/u, +/− and Ω symmetries

(j_1, j_2)	E_T (eV)	$P_{obs}(j_1, j_2)$	$P_{ad}(j_1, j_2)$	$P_{stat}(j_1, j_2)$
2, 2	1.535	0.071(3)	0	4/18=0.222
2, 1	1.515	0.554(8)	0.377	7/18=0.389
2, 0	1.507	0.102(5)	0.236 [a]	2/18=0.111
1, 1	1.495	0.095(4)	0.118 [a]	3/18=0.167
1, 0	1.487	0.175(5)	0.268	2/18=0.111
0, 0	1.479	0.003(2)	0	0/18=0

[a] The branching ratio for the $^5\Pi_u$ state dissociating to the (2, 0) and (1, 1) limits was arbitrarily chosen to be 2:1, in accordance with the degeneracy of the Ω-specific correlations (see ref. [13]).

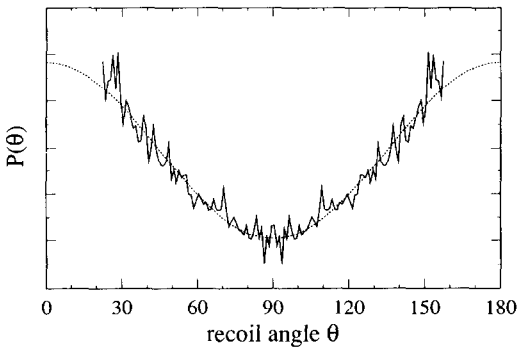

Fig. 3. The photofragment angular distribution $P(\theta)$. Also shown is the least-squares fit to the experimental data, which yielded an anisotropy parameter of $\beta = 0.76 \pm 0.03$.

value of 0.76 ± 0.03 (see fig. 3). The anisotropy of the individual spin–orbit limits were equal within experimental error. More experiments will be required to determine if this value is affected by saturation or by power broadening. However, this value of β is quite consistent with the observed 2 cm^{-1} natural linewidth for the $v' = 7$ level of the $B\,^3\Sigma_u^-$ state. The classical rotational period of this level with $N' = 4$ is 5.3 ps, comparable to the 2.7 ps predissociation lifetime. As might be expected for such a case, the observed anisotropy is intermediate between the short lifetime classical limit ($\beta = 2$) and the long lifetime, rotationally averaged classical limit ($\beta = 0.5$). A more detailed analysis is complicated by the overlap between the P(1) and R(3) transitions. In addition, the unresolved spin–rotation components of $N' = 0$ (F_1 and F_2) and $N' = 4$ (F_1, F_2 and F_3) can each be expected to couple with different strengths to the repulsive curves, resulting in spin–rotation state-specific β parameters. Nonetheless, the observed β parameter was quite reproducible. Our continuing studies of this system should make possible a more complete analysis of the anisotropy.

Before discussing these results, it is worth pointing out that the high resolution displayed in fig. 2 is possible only because of the coincidence detection scheme used in this work. This differs in principle from most photofragment translational spectroscopy experiments in which only one fragment is detected. In our experiment, for each photodissociation event, we measure the distance between the two photofragments on the detector and the time delay between their arrival. These quantities are determined to a precision of 100 μm and 0.5 ns, respectively. One could imagine a simpler scheme in which the position of only one fragment is measured relative to the center of the detector, along with the arrival time relative to the dissociation laser pulse at t_0. The energy resolution of the latter experiment would be degraded by both the size of the radical beam at the detector (about 1 mm diameter in our case) and the uncertainty in t_0 (about 20 ns). The coincidence scheme, on the other hand, is insensitive to these effects. It *is* sensitive to the spread in the laboratory kinetic energy of the ion beam. However, this spread is less than 0.1% [#1], far less than the typical energy spread (1%–10%) in most neutral molecular beam photodissociation studies. Thus, the energy resolution $\Delta E/E = 0.7\%$ in fig. 2 is limited solely by the precision with which we can measure the photofragment separation and time delay; as such, it represents the resolution of the raw data without any deconvolution over the experimental parameters.

The only single fragment detection scheme with comparable translational energy resolution is the hydrogen atom time-of-flight method developed by Welge and Ashfold [28], which provides unparalleled energy resolution of 0.3%. In this most favorable case, the laboratory-frame recoil velocity of the H atoms is largely independent of the velocity of the parent molecule, and the recoil distance is much larger than the spatial extent of the dissociation volume. We note that the ion-imaging technique developed by Chandler and Houston [29], while providing quantum state selection of one of the photofragments, actually has fairly poor translational energy resolution (0.2–0.5 eV) for the reasons given in the preceding paragraph. This limits the extent to which the undetected fragment can be characterized.

[#1] In refs. [18] and [24], the energy spread in our fast beam was increased from 0.02% to 2% by the application of a coaxial ion packet "compressor". This compressor improved the spatial and temporal overlap of the ion packets with the 30 ns laser pulses by a factor of five, while causing some degradation of the recoil energy resolution.

4. Discussion

These observations are the first correlated fine-structure state measurements for O_2 dissociation. With the exception of recent work by Robra et al. on the photodissociation of NO_2 [30], correlated fine-structure state distributions have only been measured for systems with much larger spin–orbit interactions (see, e.g. ref. [31]). They provide more detailed information about the dissociation dynamics than the uncorrelated spin–orbit state distributions for O_2 measured recently [13–15]. Matsumi and Kawasaki have reported the uncorrelated spin–orbit state distribution for the predissociation of the $v'=4$ level of the $B\,^3\Sigma_u^-$ state [14]. However, in the same publication, their reported branching ratios for Schumann–Runge continuum dissociation at 157 nm do not agree with those of Huang and Gordon [13]. No other observations of the predissociation product state distribution from bound levels of the $B\,^3\Sigma_u^-$ state have been reported.

We not consider the implications of the fine-structure distribution listed in table 1 on the determination of the predissociation mechanism(s). In order to correlate our results to the specific dissociation pathways, it is necessary to find a transformation that will map each of the repulsive states ($^3\Pi_u$, $^1\Pi_u$, $^5\Pi_u$, and $2\,^3\Sigma_u^+$) onto the asymptotic (j_1, j_2) limits. At short range ($R \approx R_e$, the equilibrium bond length for the $B\,^3\Sigma_u^-$ state), the electronic states are represented well by Hund's case (a) functions. At long range (R much larger than R_e), spin–orbit effects dominate any electrostatic interactions and Hund's case (c) functions are more appropriate. Each Hund's case (c) state will correlate to a single (j_1, j_2) limit as $R \to \infty$. The difficulty, then, occurs in the "recoupling region" ($R \approx 2$–$3R_e$), where the transition between Hund's case (a) and (c) occurs [16]. The most straightforward way to connect the case (a) and case (c) is by means of adiabatic curves, each labeled with quantum umber Ω, the projection of the total angular momentum J on the internuclear axis. The quantum number Ω is good for all R. Because of the spin–orbit interaction, these "relativistic adiabats" [32] will have avoided crossings between curves of common Ω. Given knowledge of the energy ordering of the Hund's case (a) curves at short range, a powerful correlation diagram can be constructed connecting the Ω components of the Hund's case (a) curves to single asymptotic (j_1, j_2) limits. (Only those curves with $\Omega = 0^+$ and 1 need be considered [13].) In the limit of slow recoil, the dissociation will follow the adiabatic surfaces through the recoupling region, avoiding transitions at avoided crossings between surfaces of common Ω.

With the aid of such an adiabatic correlation diagram [13], the final spin–orbit state distribution can be predicted with knowledge of relative predissociation rates into the various repulsive surfaces. Parkinson and co-workers have modeled the predissociation mechanism of the O_2 $B\,^3\Sigma_u^-$ state semi-empirically, based on their observations of the linewidths and line positions of the Schumann–Runge bands [8,9]. Their analysis predicts that the $v'=7$ level is predissociated primarily by the $2\,^3\Sigma_u^+$ and $^5\Pi_u$ states. It is reasonable to assume that under our experimental conditions, the spin–rotation fine structure sublevels F_1, F_2 and F_3 (and, therefore, the Ω components 0^+ and $1^\pm$) were excited in roughly equal proportions. Averaging over the fine structure, Parkinson and co-workers predict partial linewidths of 0.629 cm^{-1} for the $2\,^3\Sigma_u^+$ state and 0.831 cm^{-1} for the $^5\Pi_u$ state. These states correlate adiabatically to the more highly excited spin–orbit states of the $^3P_{j_1}$, $^3P_{j_2}$ limit; specifically, the $2\,^3\Sigma_u^+$ state correlates to the (1, 0) limit, while the $^5\Pi_u$ state correlates to the (2, 0) and (1, 1) limits. Parkinson and co-workers predict that the lower-energy states $^3\Pi_u$ and $^1\Pi_u$, which both correlate to the (2,1) limit, play somewhat smaller roles in the predissociation (partial widths of 0.535 and 0.348 cm^{-1}, respectively). The fourth column of table 1 lists the branching ratios predicted in the adiabatic limit following the predicted predissociation rates of Parkinson and co-workers.

Our observed (j_1, j_2) distribution has some points of agreement with these branching ratios. For example, both the experiment and the model give the (2, 1) products as the most likely pathway. However, the adiabatic correlation significantly underestimates the yield of the lowest energy products, namely, the (2, 1) and (2, 2) channels. The discrepancies between the third and fourth columns in table 1 can be due to two possible sources. The first possibility is that the assumption of adiabatic behavior in the recoupling region may be breaking

down. The second possibility is that the analysis of Parkinson and co-workers has underestimated the strength of the coupling to the $^3\Pi_u$ and $^1\Pi_u$ surfaces, which correlate to the (2, 1) limit.

The first possibility, namely, that nonadiabatic transitions are affecting the fine structure distributions, is certainly true to at least a limited extent. The clear presence of 7% of the products falling into the ground state (2, 2) limit (see fig. 2) proves that transitions between the adiabatic curves are taking place. In the adiabatic basis, the (2, 2) limit correlates only to lower-lying bound states of O_2 (namely, to $A\,^3\Sigma_u^+$, $A'\,^3\Delta_u$, and $c\,^1\Sigma_u^-$). These states cannot be playing a role in the primary predissociation mechanism. Instead, the (2, 2) products must be born at large R, where the bound states and repulsive states become nearly degenerate.

Given that some nonadiabatic transitions are occurring, it is worth examining what would happen in the case of complete mixing of the adiabatic curves with the same value of Ω. This would yield a statistical distribution of products, with the weighting of each (j_1, j_2) channel determined by its degeneracy (counting only the number of $\Omega=0^+$ and 1 states associated with each channel). Such a distribution is shown in the fifth column of table 1. It is clear that this limit reflects the observed distribution no better than the adiabatic description. The (2, 1) channel again has the most population, but is significantly underestimated in the statistical model. Furthermore, the statistical limit badly overpredicts the yield in the (2, 2) channel, which accounts only for a small fraction of the products. It is clear that the observed 55% yield of (2, 1) products is not a statistical result, but instead is a consequence of the detailed dissociation dynamics.

We consider the possibility, then, that the dissociation follows the adiabats for the most part, and that the nonadiabatic coupling can be considered as a perturbation. Nonadiabatic behavior is expected to arise when the spin–orbit splittings between the adiabatic curves are not sufficiently strong to overcome the coupling caused by motion of the recoiling O atoms. As suggested by Huang and Gordon [13], the most likely nonadiabatic mechanism is a Demkov-type transition [33–35], where the recoil is fast enough that the R dependence of the spin–orbit precession rate induces a transition between the adiabats. This argument seems plausible when one compares the kinetic energy of the O atoms (≈ 1.5 eV) to the asymptotic 0.01–0.02 eV splittings between the surfaces. The Demkov mechanism involves the purely radial motion of the nuclei and will only mix curves of common Ω. (On the other hand, the rotational motion of the nuclei ($E_{rot}=0.002$ eV for $N'=4$) is quite unlikely to contribute to the nonadiabaticity.) A rough estimate of the nonadiabatic transition probability P_{12}^{D} can be made with the aid of the Demkov formula,

$$P_{12}^{D} = \tfrac{1}{2}\,\mathrm{sech}^2(2\pi^2 H_{12}/h\nu\beta_D)\,. \qquad (3)$$

Here, H_{12} is the spin–orbit interaction between adiabatic surfaces, v is the magnitude of the recoil velocity vector, and $\beta_D \equiv \partial \ln H_{12}(R)/\partial R$. The Demkov model assumes that the coupling between surfaces increases (or falls) exponentially with R; given this assumption, a pair of interacting surfaces will have a single, R-independent value of β_D throughout the curve-crossing region.

Using estimated values of $\beta_D = 0.6$ Å^{-1} (see ref. [13]) and $H_{12} = \frac{1}{2}\Delta V = 0.01$ eV, eq. (3) predicts that nonadiabatic transitions for recoils with 1.5 eV occur 12.3% of the time. This probability is close to the 7% yield observed in the (2, 2) channel which, as mentioned above, does not correlate to any of the molecular states involved in the dissociation. Hence, it seems reasonable that this channel is populated by a nonadiabatic transition in the recoupling region, most likely from a surface which is adiabatically correlated to the (2, 1) channel, the channel which lies closest to the (2, 2) channel. However, it is still difficult to explain the large yield of (2, 1) products observed in the experiment within the framework of nonadiabatic perturbations to the adiabatic populations in table 1. Regardless of the detailed mechanism, one would expect the population resulting from such a perturbation to lie between the adiabatic and statistical limits, both of which significantly underestimate the (2, 1) yield.

An alternative explanation for the differences between the third and fourth columns off table 1 is that the adiabatic limit does not match the experimental results because the relative contributions of the various repulsive states assumed in table 1 are incorrect. Specifically, Parkinson and co-workers [8,9] may have underestimated the strength of the coupling to

the $^1\Pi_u$ and/or $^3\Pi_u$ surfaces. These are the two states that correlate adiabatically to the (2, 1) limit. In a recent study, Cosby et al. have reported linewidths for the $v'=0$ and $v'=2$ levels of the B $^3\Sigma_u^-$ state [12]. The combination of narrow linewidths and very poor Franck–Condon overlap with the X $^3\Sigma_g^-$ ($v''=0$) state had prevented the accurate measurement of these linewidths in the earlier studies; this new study provided fresh insight into the nature of strengths of the couplings to the $^3\Pi_u$ and $^1\Pi_u$ states. These new results led Parkinson and co-workers to revise their earlier $^1\Pi_u$ potential in ref. [8] and, perhaps more significantly, to increase their estimate of the spin–orbit coupling matrix element A_x from 33 cm^{-1} to 41 cm^{-1} [9]. Their revised prediction of the $^1\Pi_u$ partial predissociation width was used to derive the adiabatic distribution in the fourth column of table 1. Although, as indicated above, the agreement with our observed (j_1, j_2) distribution is not satisfactory, it is considerably better than when their older values [8] are used. In light of these recent developments, it seems possible that not enough information can be distilled from the observed B $^3\Sigma_u^- \leftarrow$ X $^3\Sigma_g^-$ line widths and positions alone to determine quantitatively the nature of the curve crossings between all four repulsive curves and the B $^3\Sigma_u^-$ state, and that a further upward revision of the $^3\Pi_u$ and $^1\Pi_u$ contributions to the predissociation rate may be necessary.

The data indicate that the dissociation dynamics are in an interesting intermediate regime between the adiabatic and statistical behavior. The dissociation is not so sudden that a statistical distribution of fine structure states arises, but it is rapid enough that transitions between the Hund's case (c) surfaces are induced. Thus, the experimental results contain information about both short-range dynamics (e.g., the surprisingly strong peak in the (2, 1) channel); the results also show the presence of long-range interactions, with the yield of ground state (2, 2) products providing a measure of the strength of nonadiabatic transitions. In principle, correlated spin–orbit distributions such as the one reported here can be used to study *both* the short-range and long-range dynamics. Toward this end, a study of the v' dependence of the correlated spin–orbit distributions is in progress.

5. Conclusions

We have presented results from a fast beam photofragment translational spectroscopy study of the predissociation of the O_2 Schumann–Runge B $^3\Sigma_u^-$ state. The relatively high-energy resolution of our coincidence time-and-position sensitive detector (10 meV for 1.5 eV recoils) allowed us to resolve the spin–orbit levels of the $^3P_{j_1}$, $^3P_{j_2}$ product states. We find that the observed (j_1, j_2) distribution is not completely consistent with dissociation along the adiabatic Hund's case (c) curves. Instead, some of the dissociation events involve nonadiabatic curve crossings. However, the structure in the observed (j_1, j_2) distribution is also inconsistent with completely statistical distribution. For this reason, it seems likely that the recent analyses of Parkinson and co-workers [8,9] have underestimated the strength of the coupling of the $^3\Pi_u$ and $^1\Pi_u$ states.

The final state distribution presents an interesting picture, showing in part the signature of the initial dissociation mechanism, but also carrying information about long-range interactions. A theoretical calculation of the detailed long-range dynamics of the Schumann–Runge B $^3\Sigma_u^-$ predissociation system and related O_2 dissociation systems will be required to fully account for the observed spin–orbit distributions. An experimental study of the spin–orbit distribution as a function of the B $^3\Sigma_u^-$ state vibrational level is in progress. These results should permit the unraveling of the short-range predissociation mechanism from the long-range exit channel interactions.

Acknowledgement

This research is supported by the Director, Office of Energy Research, Office of Basic Energy Sciences, Chemical Sciences Division, of the US Department of Energy under Contract No. DE-AC03-76SF00098. Additional support is provided by the National Science Foundation under Grant No. CHE-9108145.

References

[1] V. Schumann, Smithson. Contrib. Knowl. 29 (1903) 1413; T. Lyman, Astrophys. J. 27 (1908) 87; W. Lochte-Holtgreven and C.H. Deike, Ann. Phys. 3 (1929) 937.

[2] M. Nicolet, J. Geophys. Res. 86 (1981) 5203.
[3] B.R. Lewis, J.H. Carver, T.I. Hobbs, D.G. McCoy and H.P.F. Gies, J. Quant. Spectry. Radiative Transfer 20 (1978) 191; 22 (1979) 213;
H.P.F. Gies, S.T. Gibson, D.G. McCoy, A.J. Blake and B.R. Lewis, J. Quant. Spectry. Radiative Transfer 26 (1981) 469.
[4] B.R. Lewis, L. Berzins, J.H. Carver and S.T. Gibson, J. Quant. Spectry. Radiative Transfer 36 (1986) 187.
[5] A.S.-C. Cheung, K. Yoshino, D.E. Freeman, R.S. Friedman, A. Dalgarno and W.H. Parkinson, J. Mol. Spectry. 134 (1989) 362;
A.S.-C. Cheung, K. Yoshino, J.R. Esmond, S.S-L. Chiu, D.E. Freeman and W.H. Parkinson, J. Chem. Phys. 92 (1990) 842;
S.S.-L. Chiu, A.S.-C. Cheung, K. Yoshino, J.R. Esmond, D.E. Freeman and W.H. Parkinson, J. Chem. Phys. 93 (1990) 5539, and references therein.
[6] P.S. Julienne and M. Krauss, J. Mol. Spectry. 56 (1975) 270.
[7] P.S. Julienne, J. Mol. Spectry. 63 (1976) 60.
[8] S.S.-L. Chiu, A.S.-C. Cheung, M. Finch, M.J. Jamieson, K. Yoshino, A. Dalgarno and W.H. Parkinson, J. Chem. Phys. 97 (1992) 1787.
[9] A.S.-C. Cheung, D.K.-W. Mok, M.J. Jamieson, M. Finch, K. Yoshino, A. Dalgarno and W.H. Parkinson, J. Chem. Phys. 99 (1993) 1086.
[10] A.M. Wodtke, L. Hüwel, H. Schlüter, H. Voges, G. Meijer and P. Andresen, J. Chem. Phys. 89 (1988) 1929.
[11] X. Yang, A.M. Wodtke and L. Hüwel, J. Chem. Phys. 94 (1991) 2469.
[12] P.C. Cosby, H. Park, R.A. Copeland and T.G. Slanger, J. Chem. Phys. 98 (1993) 5117.
[13] Y.L. Huang and R.J. Gordon, J. Chem. Phys. 94 (1991) 2640.
[14] Y. Matsumi and M. Kawasaki, J. Chem. Phys. 93 (1990) 2481.
[15] K. Tonokura, N. Shafer, Y. Matsumi and M. Kawasaki, J. Chem. Phys. 95 (1991) 3394.
[16] S.J. Singer, K.F. Freed and Y.B. Band, J. Chem. Phys. 79 (1983) 6060; Advan. Chem. Phys. 61 (1985) 1.
[17] J. Durup, Chem. Phys. 59 (1981) 351.
[18] R.E. Continetti, D.R. Cyr, D.L. Osborn, D.J. Leahy and D.M. Neumark, J. Chem. Phys. 99 (1993) 2616.
[19] M.A. Johnson, M.L. Alexander and W.C. Lineberger, Chem. Phys. Letters 112 (1984) 285.
[20] J.M.B. Bakker, J. Phys. E 6 (1973) 785; 7 (1974) 364.
[21] R.J. Celotta, R.A. Bennett, J.L. Hall, M.W. Siegel and J. Levine, Phys. Rev. A 6 (1972) 631.
[22] M.J. Travers, D.C. Cowles and G.B. Ellison, Chem. Phys. Letters 164 (1989) 449.
[23] D.R. Cyr, R.E. Continetti, R.B. Metz, D.L. Osborn and D.M. Neumark, J. Chem. Phys. 97 (1992) 4937.
[24] D.J. Leahy, D.R. Cyr, D.L. Osborn and D.M. Neumark, SPIE Proceedings 1858 (1993) 49;
D.R. Cyr, D.J. Leahy, D.L. Osborn, R.E. Continetti and D.M. Neumark, J. Chem. Phys. 99 (1993), in press.
[25] D.P. de Bruijn and J. Los, Rev. Sci. Instrum. 53 (1982) 1020.
[26] R.N. Zare and D.R. Herschbach, Proc. IEEE 51 (1963) 173; R.N. Zare, Mol. Photochem. 4 (1972) 1.
[27] C.E. Moore, Atomic energy levels, Vol. 1, NSRDS-NBS circular No. 467 (US GPO, Washington, 1949) p. 15.
[28] H.J. Krautwald, L. Schnieder, K.H. Welge and M.N.R. Ashfold, Faraday Discussions Chem. Soc. 82 (1986) 99;
L. Schnieder, W. Meier, K.H. Welge, M.N.R. Ashfold and C.M. Western, J. Chem. Phys. 92 (1990) 7027;
D.H. Mordaunt, I.R. Lambert, G.P. Morley, M.N.R. Ashfold, C.M. Western, L. Schnieder and K.H. Welge, J. Chem. Phys. 98 (1993) 2054.
[29] D.W. Chandler and P.L. Houston, J. Chem. Phys. 87 (1987) 1445;
M.H.M. Janssen, D.H. Parker, G.O. Sitz, S. Stolte and D.W. Chandler, J. Phys. Chem. 95 (1991) 8007;
T. Suzuki, V.P. Hradil, S.A. Hewitt, P.L. Houston and B.J. Whitaker, Chem. Phys. Letters 187 (1991) 257;
M.A. Buntine, D.P. Baldwin and D.W. Chandler, J. Chem. Phys. 96 (1992) 5843.
[30] U. Robra, H. Zacharias and K.H. Welge, Z. Physik D 16 (1990) 175.
[31] N.J.A. van Veen, M.S. de Vries, T. Baller and A.E. de Vries, Chem. Phys. 55 (1981) 371.
[32] H. Lefebvre-Brion and R.W. Field, Perturbations in the spectra of diatomic molecules (Academic Press, New York, 1986) pp. 28–40.
[33] Yu.N. Demkov, Soviet Phys. JETP 18 (1964) 138.
[34] R.E. Olsen, Phys. Rev. A 6 (1972) 1822.
[35] M. Sizun and E.A. Gislason, J. Chem. Phys. 91 (1989) 4603.